PHYSICAL REVIEW D VOLUME 47, NUMBER 3 1 FEBRUARY 1993

Order-α_s calculations of hadronic $W^{\pm}\gamma$ and $Z\gamma$ production

J. Ohnemus
Department of Physics, University of Durham, Durham, DH1 3LE, England

(Received 17 July 1992)

Order-α_s calculations of $p\overset{(-)}{p} \rightarrow W^{\pm}\gamma + X$ and $p\overset{(-)}{p} \rightarrow Z\gamma + X$ are presented. Results are given for total cross sections and differential distributions for energies reached at the Fermilab Tevatron, CERN Large Hadron Collider, and Superconducting Super Collider. The order-α_s corrections are modest for $Z\gamma$ production but are large for $W\gamma$ production. The large corrections to $W\gamma$ production are a consequence of the radiation amplitude zero in the $W\gamma$ Born subprocess.

PACS number(s): 13.85.Qk, 12.38.Bx, 14.80.Er

I. INTRODUCTION

Studies of $W^{\pm}\gamma$ and $Z\gamma$ production at hadron colliders are important for testing the structure of the electroweak theory [1]. $W\gamma$ production can be used to test the gauge structure of the $WW\gamma$ trilinear coupling while the $Z\gamma$ process can be used to test nonstandard interactions such as compositeness of the gauge bosons. In order to perform these tests it is important to have precise calculations of hadronic $W^{\pm}\gamma$ and $Z\gamma$ production to compare with the experimental measurements.

In the standard model, the $W^{\pm}$, Z, and γ are the gauge bosons of a local SU(2)×U(1) symmetry which governs the interactions between the gauge bosons. There are important cancellations in the standard-model amplitudes for $W^{\pm}\gamma$ production which rely on the gauge structure of the $WW\gamma$ trilinear coupling. Anomalous couplings at the $WW\gamma$ vertex will enhance the $W^{\pm}\gamma$ cross section at large invariant masses [2–4]. Higher-order corrections will also enhance the cross section, thus it is imperative to include the higher-order corrections in any test of the $WW\gamma$ trilinear coupling.

The $Z\gamma$ process is also of interest as a test of the standard model even though it is not sensitive to the non-Abelian gauge couplings. Reference [5] found that the process $p\bar{p} \rightarrow Z\gamma$ is sensitive to contact interactions which appear in composite models of gauge bosons; a composite Z boson will yield enhancements in the cross section. Higher order corrections also enhance the cross section, so it is again important to include the higher-order corrections in any test of compositeness in this process.

$W\gamma$ and $Z\gamma$ production were first calculated in Refs. [6] and [7], respectively. The $W\gamma$ process has been the subject of much theoretical work since it can be used to test the gauge-boson self-coupling. The zeros in the tree-level amplitudes [8] are prominent examples of observables that are sensitive to the gauge-boson self-coupling. The magnetic dipole moment and the electric quadrupole moment of the W boson are also sensitive to the gauge-boson self-coupling. Many studies have focused on the prospects of measuring the $WW\gamma$ coupling in $p\overset{(-)}{p}$ [2–4], ep [9], and e^+e^- [10] collisions at present and future colliders. The first direct measurement of the $WW\gamma$ coupling has recently been reported by the UA2 Collaboration [11]. Bounds on the W-boson magnetic dipole moment, based on integrated total cross sections, have been given in Ref. [12]. The production of $W\gamma$ and $Z\gamma$ pairs in association with one and two jets was calculated in Refs. [13] and [14], respectively. The gluon fusion subprocess $gg \rightarrow Z\gamma$, which proceeds via a quark box loop, has been calculated in Refs. [15] and [16]. Although this process is of order α_s^2, it can be important at supercollider energies due to the large gluon luminosity; it is 15-30 % as large as the $q\bar{q} \rightarrow Z\gamma$ Born process at supercollider energies [16].

An order-α_s calculation of hadronic $W\gamma$ production was first presented in Ref. [17] where particular attention was paid to the effect of the order-α_s corrections on the amplitude zero. Numerical results were given in Ref. [17] for center-of-mass energies reached at the CERN Super Proton Synchrotron (Sp$\bar{\text{p}}$S) and the Fermilab Tevatron $p\bar{p}$ collider. Until now $Z\gamma$ production has been calculated only in the leading-logarithm (LL) approximation. Complete next-to-leading-logarithm (NLL) calculations of hadronic $W^{\pm}\gamma$ and $Z\gamma$ production are presented in this paper. At the parton level this involves computing the contributions from the 2 → 3 real emission subprocesses $q_1\bar{q}_2 \rightarrow V\gamma g$, $q_1 g \rightarrow V\gamma q_2$, and $g\bar{q}_2 \rightarrow V\gamma\bar{q}_1$ as well as the one-loop corrections to the 2 → 2 subprocess $q_1\bar{q}_2 \rightarrow V\gamma$ ($V = W^{\pm}$ or Z). The focus of the present calculations is on the order-α_s corrections and, hence, the order-α_s^2 gluon fusion contribution to $Z\gamma$ production has not been included. However, this contribution should eventually be included when calculating the full $Z\gamma$ production cross section since it can be significant at supercollider energies.

The NLL calculation presented here makes use of a combination of analytic and Monte Carlo integration methods. The same methods have been used to perform NLL calculations for hadronic ZZ [18], W^-W^+ [19], $W^{\pm}Z$ [20], and $\gamma\gamma$ [21] production, direct photon production [22], photoproduction [23], symmetric dihadron production [24], and W production [25]. The Monte Carlo approach to NLL calculations has many advantages over a purely analytic calculation. The Monte Carlo approach allows one to calculate any number of observables simultaneously by simply histogramming the appropriate quantities. Furthermore, it is easy to tailor the Monte Carlo calculation to different experimental conditions, for example, detector acceptances, experimental cuts, and jet definitions. Also, with the Monte Carlo approach one can easily study the NLL corrections for different observables, the variation of the NLL corrections in different regions of phase space, and the dependence of the NLL cross section on the choice of scale.

The procedure for the NLL $V\gamma$ calculations is identical to the procedure used in Refs. [18–21] for the NLL calculations of ZZ, W^-W^+, $W^{\pm}Z$, and $\gamma\gamma$ production. In fact, most of the expressions for the $V\gamma$ cases can be obtained from the corresponding expressions for the ZZ case by simply replacing the ZZ Born cross section with the $V\gamma$ Born cross section. The only exception to this rule is the finite virtual corrections, which must be calculated anew. Thus only the final expressions for the NLL $V\gamma$ calculations will be given in this paper. Details on the derivations of these expressions can be found in Ref. [18].

The remainder of this paper is organized as follows. Section II describes the techniques used in the Monte Carlo approach to NLL calculations. The NLL calculation of $V\gamma$ production is described in Sec. III. Results are presented in Sec. IV and summary remarks are given in Sec. V. Finally, there are three appendices containing formulas for the photon bremsstrahlung cross section, loop integrals, and the squared matrix element for the subprocess $q\bar{q} \to Z\gamma g$.

II. MONTE CARLO FORMALISM

The Monte Carlo formalism for NLL calculations has been described in detail in Refs. [18–25] so the discussion here will be brief. First of all, three-body phase space is partitioned into singular and finite regions by introducing soft and collinear cutoff parameters δ_s and δ_c, respectively. The soft region of phase space is defined to be the region where the gluon energy in the subprocess rest frame becomes less than $\delta_s\sqrt{s}_{12}/2$ and the collinear regions of phase space are defined to be those regions where any invariant (s_{ij} or t_{ij}) becomes smaller in magnitude than $\delta_c\, s_{12}$. The invariants are defined by $s_{ij} = (p_i + p_j)^2$ and $t_{ij} = (p_i - p_j)^2$ where the four-vectors of the two-body and three-body subprocesses are labeled by $p_1 + p_2 \to p_3 + p_4$ and $p_1 + p_2 \to p_3 + p_4 + p_5$. Next, the squared three-body matrix element is approximated in the singular regions; the soft gluon and leading-pole approximations are used in the soft and collinear regions, respectively. The resulting expressions are then integrated over the singular regions of phase space. At this stage the integrated expressions contain finite two-body contributions as well as singular pieces. Dimensional regularization [26] is used to isolate the singularities. The singularities from the soft region will cancel the virtual infrared singularities while the singularities from the collinear regions will be factorized into the parton distribution or photon fragmentation functions. The remainder of three-body phase space contains no singularities and the subprocesses can be evaluated in four dimensions.

The calculation now consists of finite two- and three-body contributions; all singularities have been cancelled or factorized. Both contributions depend on the values chosen for the theoretical cutoff parameters δ_s and δ_c so that each contribution by itself has no intrinsic meaning, however, when the two- and three-body contributions are combined to form a suitably inclusive observable, all dependence on the cutoff parameters cancels. The numerical results reported in this paper are insensitive to reasonable variations of the cutoff parameters.

III. NEXT-TO-LEADING-LOGARITHM FORMALISM

A. Born process

The Feynman diagrams which contribute to the Born amplitude for the reaction

$$q_1(p_1) + \bar{q}_2(p_2) \longrightarrow V(p_3) + \gamma(p_4)\,, \tag{1}$$

where $V = W^{\pm}$ or Z, are shown in Fig. 1. The Born amplitude in N dimensions is

$$\begin{aligned}\mathcal{M}^{\rm Born} = {} & \delta_{i_1 i_2}\, e^2\, \mu^{4-N}\, \epsilon^*_\mu(p_3)\, \epsilon^*_\nu(p_4) \\ & \times \sum_{\tau=\pm} g_\tau^{q_1 V q_2}\, \bar{V}(p_2)\, P_{-\tau}\, T^{\mu\nu}\, U(p_1),\end{aligned} \tag{2}$$

where $\delta_{i_1 i_2}$ is the color tensor (i_1, i_2 are color indices for quarks 1 and 2), e is the electromagnetic coupling constant, μ is a mass parameter introduced to keep the couplings dimensionless, $\epsilon^*_\mu(p_3)$ and $\epsilon^*_\nu(p_4)$ are the weak-boson and photon polarization vectors, and P_τ denotes the left-right-projection operator $P_\tau = \frac{1}{2}(1 + \tau\gamma_5)$. The left- and right-handed weak-boson-to-quark couplings are denoted by $g_\mp^{q_1 V q_2}$:

$$\begin{aligned} g_-^{q_1 W q_2} &= (g_-^{q_2 W q_1})^* = \frac{U_{q_1 q_2}}{\sqrt{2}\sin\theta_W}, \\ g_+^{q_1 W q_2} &= g_+^{q_2 W q_1} = 0, \\ g_-^{qZq} &= \frac{T_3^q}{\sin\theta_W\cos\theta_W} - Q_q\tan\theta_W, \\ g_+^{qZq} &= -Q_q\tan\theta_W, \end{aligned} \tag{3}$$

where Q_q and T_3^q denote the electric charge (in units of the proton charge e) and the third component of weak isospin of quark q, θ_W is the weak mixing angle, and $U_{q_1 q_2}$ is the Cabibbo-Kobayashi-Maskawa (CKM) quark mixing matrix. In the Feynman gauge the tensor $T^{\mu\nu}$ is

$$\begin{aligned} T^{\mu\nu} = {} & Q_1\, \gamma^\mu \frac{\not{p}_1 - \not{p}_4}{u} \gamma^\nu + Q_2\, \gamma^\nu \frac{\not{p}_1 - \not{p}_3}{t} \gamma^\mu \\ & - \frac{Q_1 - Q_2}{s - M_W^2} [(\not{p}_3 - \not{p}_4) g^{\mu\nu} + 2p_4^\mu \gamma^\nu - 2p_3^\nu \gamma^\mu]\,, \end{aligned} \tag{4}$$

where Q_1 and Q_2 are the electric charges of quarks 1 and 2 and $(Q_1 - Q_2)$ is the charge of the W boson. The third term corresponds to s-channel W-boson exchange and applies only for $W\gamma$ production; this term is not present for $Z\gamma$ production which has $Q_1 - Q_2 = 0$. The parton level kinematic invariants s, t, u are defined by

$$s = (p_1 + p_2)^2\,, \qquad t = (p_1 - p_3)^2\,, \qquad u = (p_1 - p_4)^2\,. \tag{5}$$

As explained in Ref. [18] (see also Refs. [17] and [27]), the γ_5 matrix can be eliminated from all traces, thus it is straightforward to evaluate the squared amplitudes in N dimensions. The algebra for this paper was evaluated with the computer algebra program FORM [28]. The squared amplitude summed over final-state polarizations and initial-state spins is

$$\begin{aligned} |\mathcal{M}^{\rm Born}|^2 = 8\,N_C\, e^4\, \mu^{4\epsilon}\, [|g_-^{q_1 V q_2}|^2 + |g_+^{q_1 V q_2}|^2] \\ \times \frac{(Q_1 t + Q_2 u)^2}{(t+u)^2} \\ \times \frac{1-\epsilon}{tu}\left[sM_V^2 - tu + \frac{1-\epsilon}{2}(t+u)^2 \right]\,, \end{aligned} \tag{6}$$

where N_C is the number of colors, the number of space-time dimensions is $N = 4 - 2\epsilon$, and M_V is the mass of the W or Z boson. Written in this form, the amplitude zero for the $W\gamma$ subprocess is manifest in the factor $(Q_1 t + Q_2 u)$ which vanishes when $u/t = 2$ for $W^+\gamma$ and $t/u = 2$ for $W^-\gamma$. The Born subprocess cross section is

$$d\hat{\sigma}^{\rm Born}(q_1\bar{q}_2 \to V\gamma) = \frac{1}{4}\,\frac{1}{9}\,\frac{1}{2s}\,|\mathcal{M}^{\rm Born}|^2\, d^N\Phi_2\,, \tag{7}$$

where the factors $\frac{1}{4}$ and $\frac{1}{9}$ are the spin average and color average, respectively, and two-body phase space is

$$\begin{aligned} d^N\Phi_2 = \frac{1}{8\pi}\left(\frac{4\pi}{s}\right)^{\epsilon} \frac{1}{\Gamma(1-\epsilon)} \left(1 - \frac{M_V^2}{s}\right)^{1-2\epsilon} \\ \times v^{-\epsilon}\,(1-v)^{-\epsilon}\, dv\,. \end{aligned} \tag{8}$$

The variable v is a dimensionless quantity and is related to the center-of-mass scattering angle θ^* by $v = \frac{1}{2}(1 + \cos\theta^*)$.

It is convenient to decompose the squared Born amplitude into three terms corresponding to the power of ϵ that appears in the squared amplitude [see Eq. (6)]:

$$|\mathcal{M}^{\rm Born}|^2 = |\mathcal{M}_0^{\rm Born}|^2 + \epsilon|\mathcal{M}_1^{\rm Born}|^2 + \epsilon^2|\mathcal{M}_2^{\rm Born}|^2\,; \tag{9}$$

with this decomposition the Born cross section can be written

$$d\hat{\sigma}^{\rm Born} = d\hat{\sigma}_0^{\rm Born} + \epsilon\, d\hat{\sigma}_1^{\rm Born} + \epsilon^2 d\hat{\sigma}_2^{\rm Born}\,. \tag{10}$$

This decomposition will be useful later for writing the virtual and soft corrections.

The Born cross section is obtained by convoluting the Born subprocess cross section with the parton densities and summing over the contributing partons:

$$\sigma^{\rm Born}(pp \to V\gamma) = \sum_{q_1,\,\bar{q}_2} \int d\hat{\sigma}^{\rm Born}(q_1\bar{q}_2 \to V\gamma)\Big[G_{q_1/p}(x_1, M^2)G_{\bar{q}_2/p}(x_2, M^2) + x_1 \leftrightarrow x_2\Big]dx_1 dx_2\,. \tag{11}$$

(Note that parton level cross sections are denoted with a caret over σ.) The kinematic region of interest for the $V\gamma$ production process is that where the weak boson and photon have large transverse momenta and are well isolated from the initial state collision axis. The soft and collinear singularities associated with t and/or $u = 0$ are thereby avoided. In addition to the Born contribution, there are also leading-logarithm (LL) contributions to $V\gamma$ production which come from photon bremsstrahlung processes such as $q_1 g \to V q_2$ followed by photon bremsstrahlung from the final state quark. Although the subprocess $q_1 g \to V q_2$ is formally of order $\alpha\alpha_s$, the photon fragmentation functions are of order α/α_s [29]; thus the photon bremsstrahlung process is of order α^2, as is the Born process. [The photon fragmentation functions in Eqs. (A3) and (A4) are proportional to $\alpha \ln(Q^2/\Lambda^2)$, thus they are proportional to α/α_s since $\alpha_s(Q^2) = 12\pi/[(33 - 2N_F)\ln(Q^2/\Lambda^2)]$.] Thus the LL cross section for $V\gamma$ production is

$$\sigma^{\rm LL} = \sigma^{\rm Born} + \sigma^{\rm LL}_{\rm brem}\,. \tag{12}$$

The LL bremsstrahlung cross section is given in Appendix A.

B. Virtual processes

The order-α_s virtual correction to $q_1\bar{q}_2 \to V\gamma$ comes from the interference between the Born graphs of Fig. 1 and the virtual graphs shown in Fig. 2. The interference

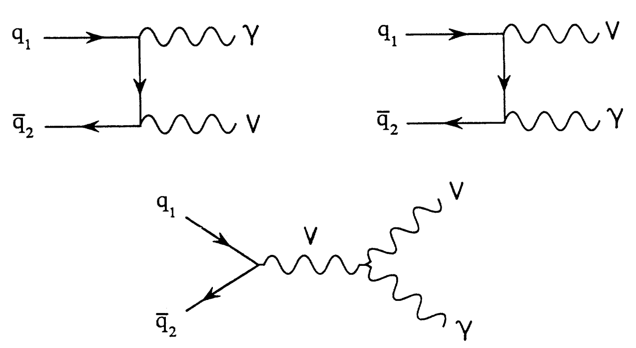

FIG. 1. Feynman diagrams for the Born subprocess $q_1\bar{q}_2 \to V\gamma$. The straight, wavy, and curly lines denote quarks, electroweak bosons, and gluons, respectively. The diagram with virtual V exchange applies only for $W\gamma$ production.

between these amplitudes has been evaluated in N dimensions using the Feynman parametrization technique. The loop integrals which occur in this calculation can be found in Refs. [18] and [19] and in Appendix B of this paper. Details of the calculational procedure can be found in Ref. [18].

The order-α_s virtual contribution to the $q_1\bar{q}_2 \to V\gamma$ cross section is

$$\begin{aligned}\frac{d\hat{\sigma}^{\rm virt}}{dv} = {} & C_F\,\frac{\alpha_s}{2\pi}\left(\frac{4\pi\mu^2}{s}\right)^{\epsilon}\frac{\Gamma(1-\epsilon)}{\Gamma(1-2\epsilon)}\left[-\frac{2}{\epsilon^2}\frac{d\hat{\sigma}_0^{\rm Born}}{dv}-\frac{2}{\epsilon}\frac{d\hat{\sigma}_1^{\rm Born}}{dv}-\frac{3}{\epsilon}\frac{d\hat{\sigma}_0^{\rm Born}}{dv}\right]\\ & +C_F\,\frac{\alpha_s}{2\pi}\,\frac{1}{4}\,\frac{1}{9}\,\frac{s-M_V^2}{16\pi s^2}N_C\,e^4\left[\left|g_-^{q_1Vq_2}\right|^2+\left|g_+^{q_1Vq_2}\right|^2\right]\frac{Q_1t+Q_2u}{t+u}[Q_1F^V(t,u)+Q_2F^V(u,t)]\,, \qquad (13)\end{aligned}$$

where $d\hat{\sigma}_0^{\rm Born}$ and $d\hat{\sigma}_1^{\rm Born}$ are defined by Eq. (10) and $C_F = \frac{4}{3}$ is the quark-gluon vertex color factor. The last term is the order-α_s finite virtual correction and the functions $F^V(t,u)$ are

$$\begin{aligned}F^W(t,u) = {} & 4\left[2\frac{s^2}{tu}+2\frac{s}{u}+\frac{t}{u}\right]H(t,u)-\frac{8}{3}\pi^2\frac{s}{t+u}\left[2\frac{s}{t}+\frac{t}{s}-\frac{u}{s}\right]\\ & +4\left[6-10\frac{u}{t+u}-10\frac{s^2}{u(t+u)}-11\frac{s}{u}-5\frac{t}{u}+2\frac{s}{t+u}+\frac{s}{s+t}\right]\\ & -4\ln\left(\frac{s}{M_W^2}\right)\left[3\frac{t}{u}+2\frac{s}{u}+4\frac{s}{u}\frac{(t+s)}{(t+u)}+2\frac{t}{u}\frac{s^2}{(t+u)^2}\right]+4\ln\left(\frac{-u}{M_W^2}\right)\left[\frac{4s+u}{s+t}+\frac{su}{(s+t)^2}\right]\,, \qquad (14)\end{aligned}$$

and

$$\begin{aligned}F^Z(t,u) = {} & 4\left[2\frac{s^2}{tu}+2\frac{s}{u}+\frac{t}{u}\right]H(t,u)-\frac{8}{3}\pi^2\frac{s^2}{tu}+4\left[1-5\frac{s^2}{tu}-11\frac{s}{u}-5\frac{t}{u}+2\frac{s}{t+u}+\frac{s}{s+t}\right]\\ & +4\ln\left(\frac{s}{M_Z^2}\right)\left[4\frac{s}{t+u}+2\frac{s^2}{(t+u)^2}-3\frac{(s+t)^2}{tu}\right]+4\ln\left(\frac{-u}{M_Z^2}\right)\left[\frac{4s+u}{s+t}+\frac{su}{(s+t)^2}\right]\,, \qquad (15)\end{aligned}$$

with

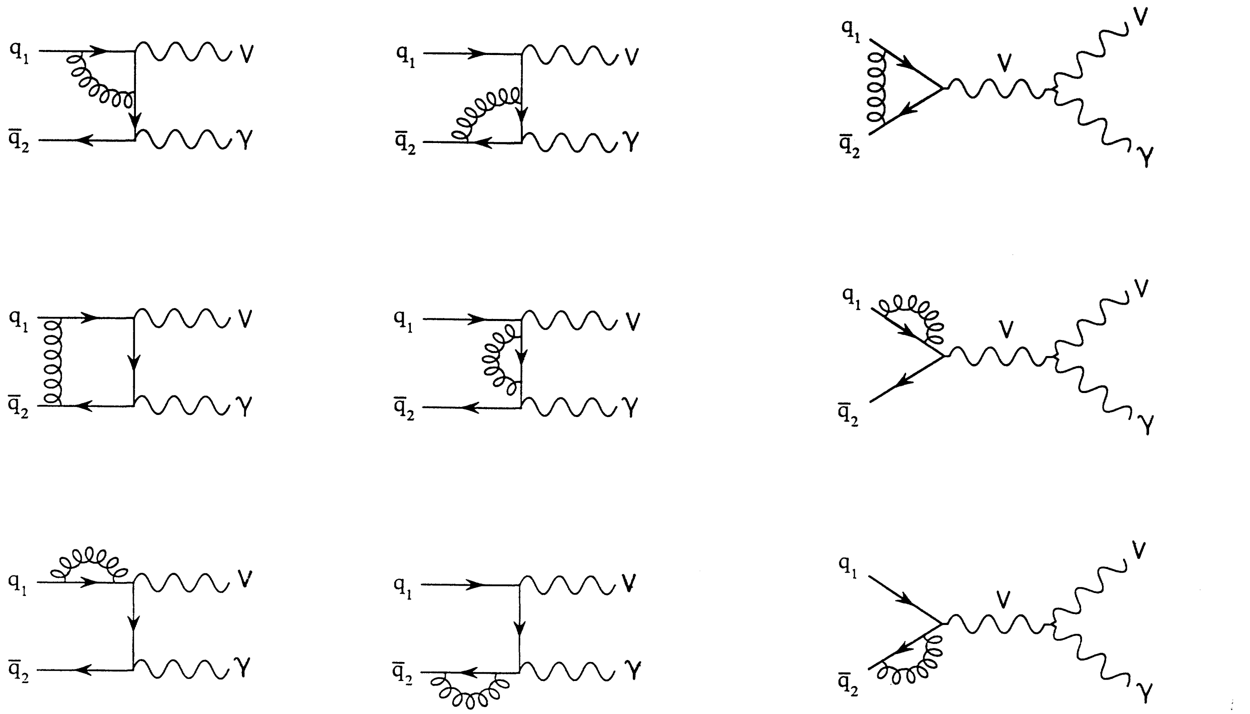

FIG. 2. Feynman diagrams for the virtual subprocess $q_1\bar{q}_2 \to V\gamma$. Not shown are the diagrams obtained by interchanging the V and γ. The diagrams with virtual V exchange apply only for $W\gamma$ production.

$$H(t,u) = \pi^2 - \ln\left(\frac{s}{M_V^2}\right)^2 + \ln\left(\frac{-u}{s}\right)^2 - \ln\left(\frac{-u}{M_V^2}\right)^2 - 2\mathrm{Li}_2\left(1 - \frac{s}{M_V^2}\right) - 2\mathrm{Li}_2\left(1 - \frac{u}{M_V^2}\right) . \tag{16}$$

The expression for the virtual correction to $W\gamma$ production agrees with the result in Ref. [17]. Note that the $W\gamma$ virtual correction vanishes at the same point in phase space as the $W\gamma$ Born amplitude. The finite correction functions for $W\gamma$ and $Z\gamma$ production are related by

$$F^W(t,u) + F^W(u,t) = F^Z(t,u) + F^Z(u,t) . \tag{17}$$

C. Soft gluon emission

The Feynman diagrams for the real emission subprocess

$$q_1(p_1) + \bar{q}_2(p_2) \longrightarrow V(p_3) + \gamma(p_4) + g(p_5) , \tag{18}$$

are shown in Fig. 3. In the soft gluon region of three-body phase space, which is defined by $E_5 < \delta_s \sqrt{s_{12}}/2$, the soft gluon contribution to the cross section is

$$\frac{d\hat{\sigma}^{\mathrm{soft}}}{dv} = C_F \frac{\alpha_s}{2\pi} \left(\frac{4\pi\mu^2}{s}\right)^{\epsilon} \frac{\Gamma(1-\epsilon)}{\Gamma(1-2\epsilon)} \left[\frac{2}{\epsilon^2} \frac{d\hat{\sigma}_0^{\mathrm{Born}}}{dv} + \frac{2}{\epsilon} \left\{ -2\ln(\delta_s) \frac{d\hat{\sigma}_0^{\mathrm{Born}}}{dv} + \frac{d\hat{\sigma}_1^{\mathrm{Born}}}{dv} \right\} \right.$$
$$\left. + 4\ln(\delta_s)^2 \frac{d\hat{\sigma}_0^{\mathrm{Born}}}{dv} - 4\ln(\delta_s) \frac{d\hat{\sigma}_1^{\mathrm{Born}}}{dv} + 2\frac{d\hat{\sigma}_2^{\mathrm{Born}}}{dv} \right] , \tag{19}$$

where δ_s is the soft cutoff parameter defined in Sec. II.

D. Hard collinear corrections

The $2 \rightarrow 3$ real emission processes have hard collinear singularities when $t_{15} \rightarrow 0$ or $t_{25} \rightarrow 0$. These singularities must be factorized and absorbed into the initial-state parton distribution functions. The collinear regions of three-body phase space are defined to be those regions where any invariant (s_{ij} or t_{ij}) becomes smaller in magnitude than $\delta_c s_{12}$, where δ_c is the collinear cutoff parameter defined in Sec. II. After the factorization is performed, the contribution from the remnants of the hard collinear singularities has the form

$$\sigma^{\mathrm{HC}} = \sum_{q_1,\bar{q}_2} \int \frac{\alpha_s}{2\pi} \frac{d\hat{\sigma}_0^{\mathrm{Born}}}{dv}(q_1\bar{q}_2 \rightarrow V\gamma)\, dv\, dx_1\, dx_2$$
$$\times \left[G_{q_1/p}(x_1,M^2) \int_{x_2}^{1-\delta_s} \frac{dz}{z} G_{\bar{q}_2/p}\left(\frac{x_2}{z},M^2\right) \tilde{P}_{qq}(z) + G_{q_1/p}(x_1,M^2) \int_{x_2}^{1} \frac{dz}{z} G_{g/p}\left(\frac{x_2}{z},M^2\right) \tilde{P}_{qg}(z) \right.$$
$$\left. + G_{\bar{q}_2/p}(x_2,M^2) \int_{x_1}^{1-\delta_s} \frac{dz}{z} G_{q_1/p}\left(\frac{x_1}{z},M^2\right) \tilde{P}_{qq}(z) + G_{\bar{q}_2/p}(x_2,M^2) \int_{x_1}^{1} \frac{dz}{z} G_{g/p}\left(\frac{x_1}{z},M^2\right) \tilde{P}_{qg}(z) \right] , \tag{20}$$

with

$$\tilde{P}_{ij}(z) \equiv P_{ij}(z) \ln\left(\frac{1-z}{z}\delta_c \frac{s}{M^2}\right) - P'_{ij}(z) - \lambda_{\mathrm{FC}} F_{ij}(z) . \tag{21}$$

The Altarelli-Parisi splitting functions in $N = 4 - 2\epsilon$ dimensions for $0 < z < 1$ are

$$P_{qq}(z,\epsilon) = C_F \left[\frac{1+z^2}{1-z} - \epsilon(1-z)\right] , \tag{22}$$

$$P_{qg}(z,\epsilon) = \frac{1}{2(1-\epsilon)} \left[z^2 + (1-z)^2 - \epsilon\right] , \tag{23}$$

and can be written

$$P_{ij}(z,\epsilon) = P_{ij}(z) + \epsilon P'_{ij}(z) , \tag{24}$$

which defines the P'_{ij} functions. The functions F_{qq} and F_{qg} depend on the choice of factorization convention and the parameter λ_{FC} specifies the factorization convention; $\lambda_{\mathrm{FC}} = 0$ for the universal [modified minimal subtraction ($\overline{\mathrm{MS}}$) [30]] convention and $\lambda_{\mathrm{FC}} = 1$ for the physical [deep-inelastic scattering (DIS)] convention. For the physical convention the factorization functions are

$$F_{qq}(z) = C_F \left[\frac{1+z^2}{1-z} \ln\left(\frac{1-z}{z}\right) - \frac{3}{2}\frac{1}{1-z} + 2z + 3\right] , \tag{25}$$

$$F_{qg}(z) = \frac{1}{2}\left[\{z^2 + (1-z)^2\}\ln\left(\frac{1-z}{z}\right) + 8z(1-z) - 1\right]. \tag{26}$$

The transformation between the $\overline{\text{MS}}$ and DIS schemes is discussed in Ref. [31]. The parameter M^2 is the factorization scale which must be specified in the process of factorizing the collinear singularity. Basically, it determines how much of the collinear term is absorbed into the various parton distributions.

The upper limit on the integrals appearing in Eq. (20) is determined by requiring that the hard collinear term not overlap with the soft region previously discussed. If such an overlap were to occur, then that region of three-body phase space would be counted twice.

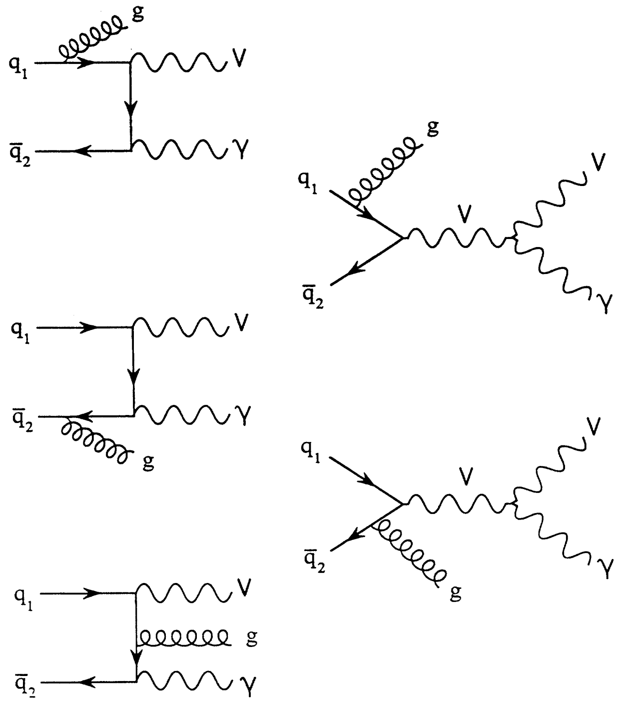

FIG. 3. Feynman diagrams for the real emission subprocess $q_1\bar{q}_2 \to V\gamma g$. Not shown are the diagrams obtained by interchanging the V and γ. The diagrams with virtual V exchange apply only for $W\gamma$ production.

E. Soft collinear subtraction term

The M^2-dependent subtraction piece which is used to absorb the collinear singularity into the parton distribution functions involves an integral over splitting functions with the upper limit corresponding to $z = 1$, not $1 - \delta_s$. Therefore, there is one last piece to be subtracted which, for the t_{15} case, has the form

$$\frac{d\sigma_{15}^{\text{SC}}}{dv} = \sum_{q_1,\bar{q}_2}\int dx_1\,dx_2\,\frac{d\hat{\sigma}^{\text{Born}}}{dv}\,\frac{\alpha_s}{2\pi}\left(\frac{4\pi\mu^2}{M^2}\right)^{\epsilon}\frac{\Gamma(1-\epsilon)}{\Gamma(1-2\epsilon)}\,G_{\bar{q}/p}(x_2,M^2) \times\int_{1-\delta_s}^{1}\frac{dz}{z}\left\{-\frac{1}{\epsilon}P_{qq}(z) + \lambda_{\text{FC}}F_{qq}(z)\right\}G_{q/p}\left(\frac{x_1}{z},M^2\right). \tag{27}$$

Inserting P_{qq} and F_{qq} and integrating yields

$$\frac{d\sigma_{15}^{\text{SC}}}{dv} = -C_F\sum_{q_1,\bar{q}_2}\int dx_1\,dx_2\,\frac{\alpha_s}{2\pi}\left(\frac{4\pi\mu^2}{s}\right)^{\epsilon}\frac{\Gamma(1-\epsilon)}{\Gamma(1-2\epsilon)} \times\left[\frac{1}{\epsilon}\left\{\frac{3}{2}+2\ln(\delta_s)\right\}\frac{d\hat{\sigma}_0^{\text{Born}}}{dv} + \left\{\frac{3}{2}+2\ln(\delta_s)\right\}\left\{\ln\left(\frac{s}{M^2}\right)\frac{d\hat{\sigma}_0^{\text{Born}}}{dv} + \frac{d\hat{\sigma}_1^{\text{Born}}}{dv}\right\} + \lambda_{\text{FC}}\left\{\frac{9}{2}+\frac{\pi^2}{3}+\frac{3}{2}\ln(\delta_s) - \ln(\delta_s)^2\right\}\frac{d\hat{\sigma}_0^{\text{Born}}}{dv}\right]G_{q/p}(x_1,M^2)\,G_{\bar{q}/p}(x_2,M^2)\,, \tag{28}$$

where terms proportional to a power of the soft cutoff δ_s have been discarded. The corresponding parton level cross section is

$$\frac{d\hat{\sigma}_{15}^{\text{SC}}}{dv} = -C_F\,\frac{\alpha_s}{2\pi}\left(\frac{4\pi\mu^2}{s}\right)^{\epsilon}\frac{\Gamma(1-\epsilon)}{\Gamma(1-2\epsilon)}\left[\frac{1}{\epsilon}\left\{\frac{3}{2}+2\ln(\delta_s)\right\}\frac{d\hat{\sigma}_0^{\text{Born}}}{dv} + \left\{\frac{3}{2}+2\ln(\delta_s)\right\}\left\{\ln\left(\frac{s}{M^2}\right)\frac{d\hat{\sigma}_0^{\text{Born}}}{dv} + \frac{d\hat{\sigma}_1^{\text{Born}}}{dv}\right\} + \lambda_{\text{FC}}\left\{\frac{9}{2}+\frac{\pi^2}{3}+\frac{3}{2}\ln(\delta_s) - \ln(\delta_s)^2\right\}\frac{d\hat{\sigma}_0^{\text{Born}}}{dv}\right]. \tag{29}$$

The soft collinear singularity in the $t_{25} \to 0$ region yields an identical result.

F. Next-to-leading-logarithm cross section

The NLL cross section, which consists of two- and three-body contributions, can now be assembled from the pieces described in the previous sections. The two-body contribution is

$$\sigma^{\rm NLL}_{2\ \rm body}(pp \to V\gamma) = \sigma^{\rm NLL}_{\rm brem} + \sigma^{\rm HC} + \sum_{q_1,\bar{q}_2} \int dv\, dx_1\, dx_2 \times \left[G_{q_1/p}(x_1, M^2)\, G_{\bar{q}_2/p}(x_2, M^2)\, \frac{d\hat{\sigma}^{\rm NLL}}{dv}(q_1\bar{q}_2 \to V\gamma) + (x_1 \leftrightarrow x_2) \right], \tag{30}$$

where the NLL bremsstrahlung cross section is defined in Appendix A, the sum is over all contributing quark flavors, $\sigma^{\rm HC}$ is defined in Eq. (20), and

$$\frac{d\hat{\sigma}^{\rm NLL}}{dv}(q_1\bar{q}_2 \to V\gamma) = \frac{d\hat{\sigma}^{\rm Born}}{dv} + \frac{d\hat{\sigma}^{\rm virt}}{dv} + \frac{d\hat{\sigma}^{\rm soft}}{dv} - \frac{d\hat{\sigma}^{\rm SC}_{15}}{dv} - \frac{d\hat{\sigma}^{\rm SC}_{25}}{dv}\,. \tag{31}$$

The $\frac{1}{\epsilon^2}$ and $\frac{1}{\epsilon}$ poles cancel when the terms in Eq. (31) are summed [see Eqs. (7), (13), (19), and (29)].

The three-body contribution to the cross section is

$$\sigma_{3\ \rm body}(pp \to V\gamma + X) = \sum_{a,b,c} \int d\hat{\sigma}(ab \to V\gamma c) \left[G_{a/p}(x_1, M^2)\, G_{b/p}(x_2, M^2) + (x_1 \leftrightarrow x_2) \right] dx_1\, dx_2\,, \tag{32}$$

where the sum is over all partons contributing to the three subprocesses $q_1\bar{q}_2 \to V\gamma g$, $q_1 g \to V\gamma q_2$, and $g\bar{q}_2 \to V\gamma\bar{q}_1$. The squared matrix elements for the $2 \to 3$ $W\gamma$ subprocesses were evaluated numerically via helicity amplitude methods as described in Ref. [14] and the squared matrix elements for the $2 \to 3$ $Z\gamma$ subprocesses are given in Appendix C. The integration over three-body phase space and $dx_1\, dx_2$ is done numerically by standard Monte Carlo techniques. The kinematic invariants s_{ij} and t_{ij} are first tested for soft and collinear singularities. If an invariant for a subprocess falls in a soft or collinear region of phase space, the contribution from that subprocess is not included in the cross section.

IV. RESULTS

Unless otherwise stated, the numerical results presented in this section have been obtained using the two-loop expression for α_s. The QCD scale $\Lambda_{\rm QCD}$ is specified for four flavors of quarks by the choice of parton distribution functions and is adjusted whenever a heavy-quark threshold is crossed so that α_s is a continuous function of Q^2. The heavy-quark masses were taken to be $m_b = 5$ GeV and $m_t = 140$ GeV ([32]). The standard-model parameters were taken to be $M_Z = 91.17$ GeV, $M_W = 80.0$ GeV, $\alpha(M_W) = 1/128$, and $\sin^2\theta_W = 1 - (M_W/M_Z)^2$. These mass values are consistent with recent measurements at the Tevatron [33], the SLAC Linear Collider [34], and the CERN e^+e^- collider LEP [35]. The soft and collinear cutoff parameters were taken to be $\delta_s = 10^{-2}$ and $\delta_c = 10^{-3}$. The parton subprocesses have been summed over u, d, c, and s quarks and the Cabibbo mixing angle has been chosen such that $\cos^2\theta_C = 0.95$. Except where otherwise stated, a single scale $Q^2 = M^2_{V\gamma}$, where $M_{V\gamma}$ is the invariant mass of the $V\gamma$ pair, has been used for the renormalization scale μ^2 and the factorization scale M^2.

The numerical results for the order α_s calculation of $W\gamma$ production have been compared with updated results from Ref. [17]. (The original calculation in Ref. [17] was recently found to contain a few minor errors [36] which will be corrected in an upcoming paper [37].) The results agree when the leading-log fragmentation functions $D^{\rm LL}_{\gamma/q}(z)$ and $D^{\rm LL}_{\gamma/g}(z)$ [see Eqs. (A3) and (A4)] are set to zero. The leading-log fragmentation functions must be set to zero because the leading-log bremsstrahlung contribution was not included in Ref. [17]. Also, when comparing with Ref. [17] in the DIS scheme, the factorization function $F_{qg}(z)$ in Eq. (26) must be replaced by

$$F_{qg}(z) = \frac{1}{2}\left[\{z^2 + (1-z)^2\} \ln\left(\frac{1-z}{z}\right) + 6z(1-z) \right], \tag{33}$$

which is the form used in Ref. [17]. [Equations (26) and (33) differ due to the convention used for the gluon spin average; $\frac{1}{N-2}$ was used for the gluon spin average in Eq. (26) whereas $\frac{1}{2}$ was used in Eq. (33).]

In order to get consistent NLL results it is necessary to use parton distribution functions which have been fit to next-to-leading order. The Harriman-Martin-Roberts-Stirling (HMRS) [38] set-B distributions with $\Lambda_4 = 190$ MeV will be used here since they fit the present data the best. Note that the HMRS distributions are defined in the universal ($\overline{\rm MS}$) scheme and thus the factorization defining parameter $\lambda_{\rm FC}$ in Eqs. (21) and (29) should be $\lambda_{\rm FC} = 0$. For convenience, the HMRS set-B distributions have also been used for the LL calculations although, strictly speaking, one should use a leading-order parameterization of the parton distributions for LL calculations.

To leading order, $V\gamma$ final states are produced via the Born process $q_1\bar{q}_2 \to V\gamma$ and by the photon bremsstrahlung process which proceeds via subprocesses such as $q_1 g \to V q_2$ followed by photon bremsstrahlung from the final-state quark. The Born and photon bremsstrahlung cross sections for $V\gamma$ production are compared in Fig. 4. The photon and weak boson were required to satisfy

$$p_T(\gamma) > 50 \text{ GeV}, \qquad |y(\gamma)| < 2.5\,, \qquad |y(V)| < 2.5\,. \tag{34}$$

These values were chosen because they are typical of experimental acceptance cuts; furthermore, the cuts on the photon transverse momentum and photon rapidity are necessary to regulate the soft and collinear divergences associated with the photon. For this figure, α_s was evaluated with the one-loop expression and $Q^2 = s_{12}$ was chosen for the scale. The figure shows that the photon bremsstrahlung process becomes more important with increasing center-of-mass energy, and in the $W\gamma$ cases, is the dominant production mechanism at large center-of-mass energies. For most cases of interest, for example, in tests of the triple weak-boson vertex, the photon bremsstrahlung process is a background to the more interesting Born process. Fortunately, the photon bremsstrahlung events can be suppressed by requiring the photon to be isolated. A photon isolation cut typically requires the sum of the hadronic energy E_{had} in a cone of size R_0 about the direction of the photon to be less than a fraction ϵ_h of the photon energy E_γ, i.e.,

$$\sum_{\Delta R < R_0} E_{\text{had}} < \epsilon_h \, E_\gamma\,, \tag{35}$$

with $\Delta R = [(\Delta\phi)^2 + (\Delta\eta)^2]^{1/2}$. The quantities $\Delta\phi$ and $\Delta\eta$ are the differences in azimuthal angle and pseudorapidity between the photon and hadron. In the photon bremsstrahlung process, the photon is emitted collinear to the final-state parton and carries a fraction z of the parent parton's momentum, thus the cone size is irrelevant and the isolation requirement reduces to a restriction on the range of the splitting fraction z. The range of the splitting fraction is reduced from $0 \le z \le 1$ to $\frac{1}{1+\epsilon_h} \le z \le 1$. The effect of a photon isolation cut is illustrated in Fig. 4 by the dotted curve which corresponds to the photon bremsstrahlung cross section with a photon isolation cut of $\epsilon_h = 0.15$. The isolation cut reduces the photon bremsstrahlung cross section by about an order of magnitude, while the Born result is unaffected. Therefore, to suppress the photon bremsstrahlung background, a photon isolation cut will be applied in the rest of the results presented in this section. Note that the LL cross section, which is the sum of the Born and photon bremsstrahlung cross sections, depends quite strongly on the photon isolation cut.

Two other features of Fig. 4 are worth noting. First, note that the $W\gamma$ Born cross section is smaller than the $Z\gamma$ Born cross section. One would naively expect just the opposite because the W-boson-to-quark coupling is larger than the Z-boson-to-quark coupling; indeed, this is the case for the photon bremsstrahlung processes. The Born cross section for $W\gamma$ production is smaller than the Born cross section for $Z\gamma$ production because the $W\gamma$ subprocess is suppressed by an amplitude zero [8]. This amplitude zero will have important consequences in the order-α_s corrections to $W\gamma$ production. The other feature to note is that the $W^-\gamma$ bremsstrahlung cross section is slightly larger than the $W^+\gamma$ bremsstrahlung cross section. In pp collisions the cross section for W^+ production is slightly larger than the cross section for W^- production because the density of u valence quarks is greater than the density of d valence quarks in the proton. On the other hand, the probability of photon bremsstrahlung is greater in the $dg \to W^- u$ subprocess than in the $ug \to W^+ d$ subprocess due to the larger electric charge of the u quark. In the end, the effect of the quark charge dominates and the $W^-\gamma$ bremsstrahlung cross section is slightly larger than the $W^+\gamma$ bremsstrahlung cross section.

Figure 5 shows the LL and NLL total cross sections as functions of the center-of-mass energy; parts (a), (b), and (c) are for $Z\gamma$, $W^+\gamma$, and $W^-\gamma$, respectively. In addition to the cuts in Eq. (34), a photon isolation cut

$$\sum_{\Delta R < 0.4} E_{\text{had}} < 0.15\, E_\gamma \tag{36}$$

has been imposed for this figure. The figure shows that the order-α_s corrections are positive and increase with the center-of-mass energy. For $Z\gamma$ production, the ratio of NLL/LL cross sections varies from 1.3 to 1.5. These

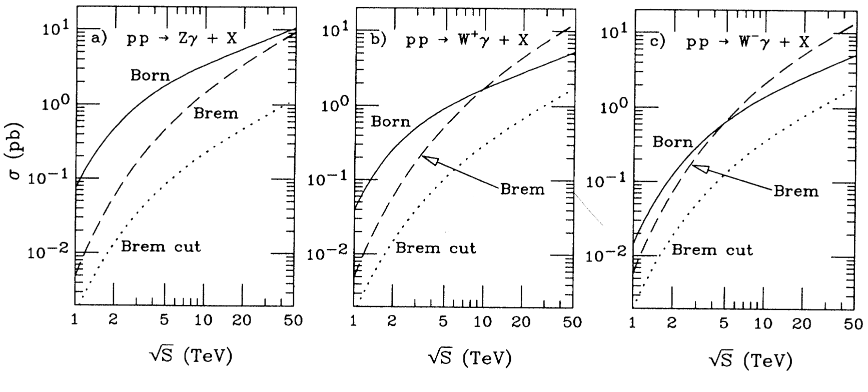

FIG. 4. The Born and photon bremsstrahlung cross sections for $pp \to V\gamma + X$ as a function of the center-of-mass energy; parts (a), (b), and (c) are for $Z\gamma$, $W^+\gamma$, and $W^-\gamma$ production, respectively. The solid curve is the Born cross section, the dashed curve is the photon bremsstrahlung cross section, and the dotted curve is the photon bremsstrahlung cross section with a photon isolation cut as described in the text.

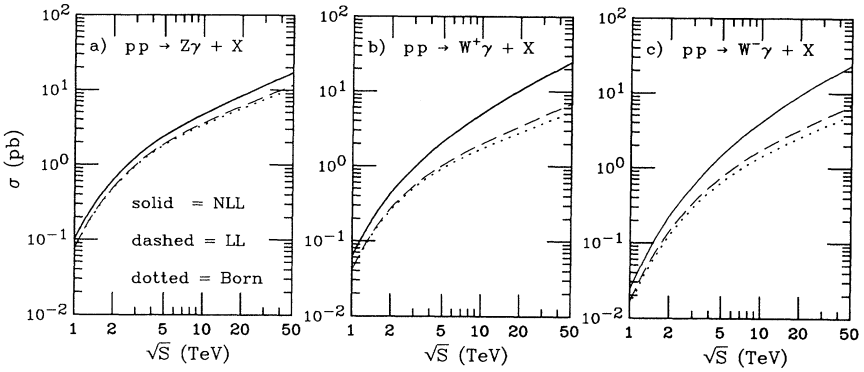

FIG. 5. Total cross section for $pp \to V\gamma + X$ as a function of the center-of-mass energy; parts (a), (b), and (c) are for $Z\gamma$, $W^+\gamma$, and $W^-\gamma$ production, respectively. The solid curve is the NLL result, the dashed curve is the LL result, and the dotted curve is the Born result.

NLL results are quantitatively similar to the NLL results for hadronic ZZ [18], W^-W^+ [19], and $W^\pm Z$ [20] production. The size of the order-α_s corrections in the $W\gamma$ processes is a bit surprising at first sight; the ratio of NLL/LL cross sections is 2.9 and 3.5 at energies reached at the LHC and SSC, respectively.

To understand the size of the order-α_s corrections in $W\gamma$ production, it is instructive to examine the behavior of the 2 → 2 and 2 → 3 tree-level cross sections for $W^+\gamma$ and $Z\gamma$ production. Figure 6(a) compares the 2 → 2 cross sections and shows that the $W^+\gamma$ Born cross section is smaller than the $Z\gamma$ cross section even though the W-boson-to-quark coupling is larger than the Z-boson-to-quark coupling. The $W\gamma$ cross section is suppressed due to destructive interference between the t-, u-, and s-channel diagrams in Fig. 1. This destructive interference, which is also responsible for the radiation amplitude zero, manifests itself in Eq. (6) in the factor

$$\frac{(Q_1 t + Q_2 u)^2}{(t+u)^2} . \tag{37}$$

For $Z\gamma$ production, which does not have the s-channel diagram, this factor reduces to Q_q^2, whereas for $W^\pm\gamma$ production this factor can be written

$$\frac{1}{4}\left(\frac{1}{3} \pm \cos\theta^*\right)^2 , \tag{38}$$

with θ^* the angle between the quark q_1 and the photon in the parton center-of-mass frame. This factor suppresses the $W^\pm\gamma$ Born cross section relative to the $Z\gamma$ Born cross section for most values of $\cos\theta^*$. The vanishing of the $W^\pm\gamma$ Born cross section at $\cos\theta^* = \mp\frac{1}{3}$ has been understood in terms of the antennae pattern for radiation from classical charge distributions [8]. Not only is the $W\gamma$ Born cross section suppressed, but in addition, all of the $W\gamma$ two-body contributions are suppressed (with the exception of the bremsstrahlung contribution which is suppressed by the photon isolation cut) since they are either proportional to the Born cross section or they contain the suppression factor $(Q_1 t + Q_2 u)$ [see Eqs. (7), (13), (19), (20), and (29)]. Thus the magnitude of the two-body contribution is smaller for $W\gamma$ production than for $Z\gamma$ production.

Figure 6(b) compares the 2 → 3 cross sections for $Z\gamma$ and $W^+\gamma$ production. The cross sections have been decomposed into contributions from $q\bar{q}$ and $qg + \bar{q}g$ initial states. The $qg + \bar{q}g$ contribution is larger for $W^+\gamma$ than for $Z\gamma$ due to the larger W-boson-to-quark coupling. In contrast, the $q\bar{q}$ contributions are nearly equal, implying that the $q_1\bar{q}_2 \to W\gamma g$ subprocess is suppressed relative to the $q\bar{q} \to Z\gamma g$ subprocess. This suppression is also due to destructive interference from the s-channel diagrams. In fact, in the soft gluon limit, the $q_1\bar{q}_2 \to W\gamma g$ subprocess has an amplitude zero [see Eq. (19)]. (An amplitude zero only occurs when all the charged particles in the subprocess have the same sign charge, thus the $q_1 g \to W\gamma q_2$ subprocess cannot have an amplitude zero.) The total 2 → 3 cross section is larger for $W\gamma$ production than for $Z\gamma$ production due to the larger W-boson-to-quark coupling. These behaviors of the tree-level cross sections were also observed in Refs. [13] and [14].

In the present calculation, the NLL cross section is

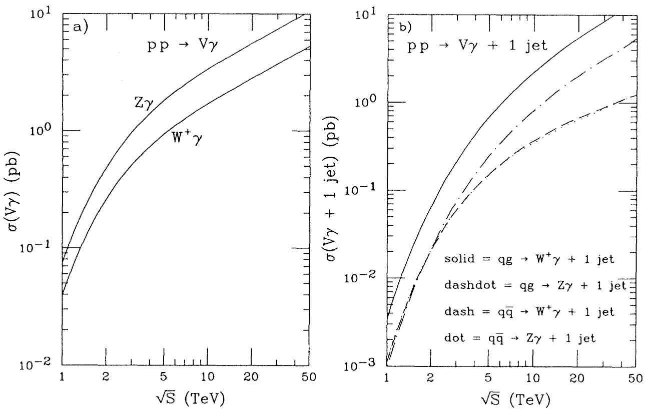

FIG. 6. Tree-level cross sections as a function of the center-of-mass energy. Part (a) is for the 2 → 2 processes $pp \to Z\gamma$ and $pp \to W^+\gamma$. Part (b) is for the 2 → 3 processes $pp \to V\gamma + 1$ jet; the cross sections have been decomposed into $q\bar{q}$ and qg initial-state components. The components are $qg \to W^+\gamma + 1$ jet (solid line), $qg \to Z\gamma + 1$ jet (dash-dotted line), $q\bar{q} \to W^+\gamma + 1$ jet (dashed line), and $q\bar{q} \to Z\gamma + 1$ jet (dotted line). This figure was made using the one-loop expression for α_s and the cuts in Eq. (34); in addition, the jet must satisfy $p_T(j) > 50$ GeV, $|y(j)| < 2.5|$, and $\Delta R(\gamma, j) > 0.4$.

given by the sum of a two-body contribution, which is negative for most values of the cutoff parameters δ_s and δ_c, and a three-body contribution, which is positive definite. The destructive interference in the $W\gamma$ Born process causes the magnitude of the two-body $W\gamma$ contribution to be about half as large as the two-body $Z\gamma$ contribution. On the other hand, the larger W-boson-to-quark coupling causes the three-body $W\gamma$ contribution to be about twice as large as the three-body $Z\gamma$ contribution. The net result is that the order-α_s corrections and cross sections are about twice as large for $W\gamma$ production than they are for $Z\gamma$ production.

In both $Z\gamma$ and $W\gamma$ production, the order-α_s corrections increase with the center-of-mass energy. The source of these corrections is illustrated in Fig. 7 where the NLL results have been decomposed into the Born contribution and the order-α_s corrections from $q\bar{q}$ and qg initial states. The order-α_s $q\bar{q}$ corrections are approximately proportional to the Born cross section; however, the order-α_s qg corrections increase rapidly with the center-of-mass energy. This rapid increase is due to the rapidly increasing gluon density at large center-of-mass energies. Thus the bulk of the order-α_s corrections is due to the opening of the $qg \to V\gamma + X$ process at order α_s and to the large gluon density at large center-of-mass energies.

The large order-α_s corrections to hadronic $W\gamma$ production raise questions about the size of the order-α_s^2 corrections and the convergence of the perturbation series. Tree-level calculations of $W\gamma + 0, 1$, and 2 jets suggest that the perturbation series is well behaved [14]. These calculations show that the 0-jet cross section (the Born cross section) is smaller than the 1-jet cross section due to the amplitude-zero suppression in the 0-jet case. On the other hand, the 2-jet cross section is smaller than the 1-jet cross section as expected, due to the extra power of α_s in the 2-jet cross section. Thus the order-α_s tree level and complete cross sections have similar behaviors. There is no reason to expect any difference in behavior between the order-α_s^2 tree level and complete cross sections. Thus the large order-α_s corrections to hadronic $W\gamma$ production do not seem to represent a breakdown of the perturbation series, but instead are only an aberration due to the suppression of the Born cross section by the radiation amplitude zero.

One of the motivations for performing NLL calculations is that the results often show a less dramatic dependence on the renormalization and factorization scale than the LL result. The scale dependence of the $Z\gamma$ and $W^{+}\gamma$ cross sections are illustrated in Figs. 8 and 9, respectively, where the total cross sections are plotted verses the scale Q. The scale Q has been used for both the renormalization and factorization scales. Parts (a), (b), and (c) are for the Tevatron, LHC, and SSC center-of-mass energies, respectively. The LHC and SSC results include the cuts of Eqs. (34) and (36) whereas the Tevatron results include the cuts

$$p_T(\gamma) > 10 \text{ GeV}, \quad |y(\gamma)| < 1.0\,, \quad |y(V)| < 2.5\,, \tag{39}$$

$$\sum_{\Delta R < 0.7} E_{\text{had}} < 0.15\, E_\gamma\,.$$

At the LL level, the scale dependence enters through the scale dependence of the parton distribution functions. The qualitative differences between the results at the Tevatron and the supercolliders are due to the differences between $p\bar{p}$ versus pp scattering and the ranges of the x values. At the Tevatron, $V\gamma$ production in $p\bar{p}$ collisions is dominated by valence-quark interactions. The valence-quark distributions have little Q^2 dependence for the x values probed at the Tevatron. On the other hand, at the LHC and SSC, sea-quark interactions dominate in the pp process and smaller x values are probed. The sea-quark distributions increase with Q^2 for the x values probed at the LHC and SSC. Thus the LL cross sections show little variation with Q^2 at the Tevatron but increase with Q^2 at the LHC and SSC. At the NLL level additional scale dependence enters via the running α_s which decreases with Q^2. The Tevatron results are examples of observables whose scale dependence increases at the NLL level. Other observables with this behavior have been encountered in the higher-order calculation of direct photon production [22]. The combination of nearly scale-independent parton distributions and decreasing α_s leads to NLL results that are decreasing with Q^2 at the Tevatron. The NLL results at the LHC and SSC exhibit the more typical behavior of decreased scale dependence. This is because the parton distributions, which are increasing with Q^2, are compensated by the running α_s which decreases with Q^2.

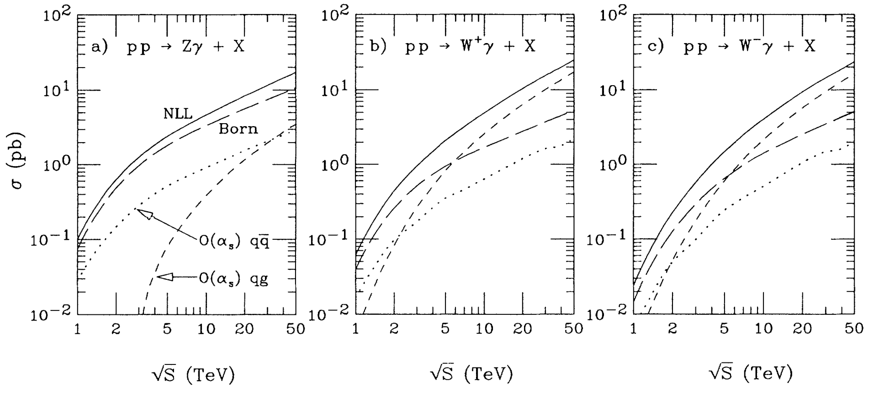

FIG. 7. Decomposition of the total cross section for $pp \to V\gamma + X$ as a function of the center-of-mass energy; parts (a), (b), and (c) are for $Z\gamma$, $W^{+}\gamma$, and $W^{-}\gamma$ production, respectively. The NLL cross section (solid line) is decomposed into the Born contribution (long dashed line), the order-α_s $q\bar{q}$ initial-state contribution (dotted line), and the order-α_s qg initial state contribution (short dashed line).

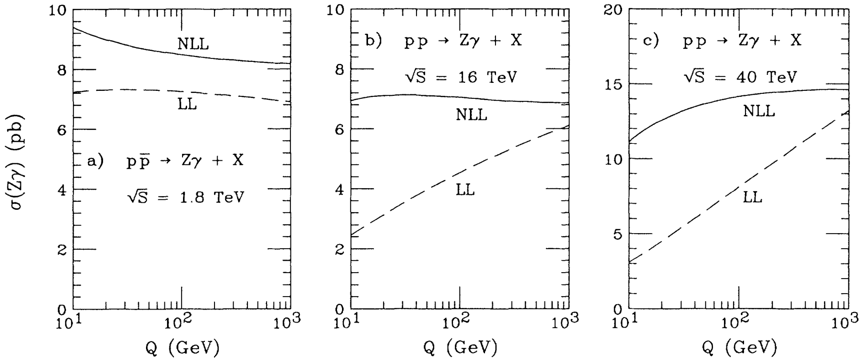

FIG. 8. The total cross section for $Z\gamma$ production as a function of the scale Q; parts (a), (b), and (c) are for the Tevatron, LHC, and SSC center-of-mass energies, respectively. The solid curve is the NLL result and the dashed curve is the LL result.

One of the major advantages of using Monte Carlo methods for NLL calculations is that one can calculate any number of differential distributions simultaneously by simply histogramming the quantity of interest. Differential distributions for $V\gamma$ production at the Tevatron and SSC center-of-mass energies are given in Figs. 10–17; parts (a) and (b) of these figures are for $Z\gamma$ and $W^+\gamma$ production, respectively. The NLL and LL results are shown in these figures. For clarity, the Born results are not shown in most cases since they are just slightly smaller than the LL results. Results for the LHC center-of-mass energy are qualitatively similar to the SSC results, but with normalizations scaled down by a factor of about 0.5. The SSC results include the cuts of Eqs. (34) and (36) whereas the Tevatron results include the cuts of Eq. (39).

The transverse momentum distributions of the photon in the processes $p\bar{p} \to V\gamma + X$ at the Tevatron energy are shown in Fig. 10. The order-α_s corrections are positive, increase with $p_T(\gamma)$, and are larger in the $W^+\gamma$ case. Both the LL and NLL cross sections for $W^+\gamma$ production are smaller than the corresponding cross sections for $Z\gamma$ production. The $p_T(\gamma)$ distributions at the SSC energy are shown in Fig. 11. The LL cross section for $W^+\gamma$ production is again smaller than the LL cross section for $Z\gamma$ production, but the situation is reversed for the NLL results. The order-α_s corrections are much larger at this energy, especially in the $W^+\gamma$ case. This behavior of the NLL result is attributed to the amplitude zero in the $W^+\gamma$ process, the opening of the $qg \to V\gamma + X$ production process at order α_s, and to the large gluon density.

Figure 12 is the $\cos\theta_\gamma$ distribution of the photon in the processes $p\bar{p} \to V\gamma + X$ at the Tevatron energy. The angle θ_γ is the angle in the laboratory frame between the proton beam and the photon. The distribution is symmetric about $\cos\theta_\gamma = 0$ for the $Z\gamma$ case, but is asymmetric in the $W^+\gamma$ case due to the amplitude zero. At the parton level, the amplitude for $q_1\bar{q}_2 \to W^+\gamma$ vanishes at $\cos\theta^* = -\frac{1}{3}$, where θ^* is the angle between the quark q_1 and the photon in the parton center-of-mass frame. At the hadron level, this zero is smeared out into a dip at $\cos\theta_\gamma = -\frac{1}{3}$. Thus the $\cos\theta_\gamma$ distribution is asymmetric, with the photon preferring to be emitted in the direction of the proton beam. The $\cos\theta_\gamma$ distribution at the SSC energy is shown in Fig. 13. In this case the $Z\gamma$ and $W^+\gamma$ distributions are both symmetric about $\cos\theta_\gamma = 0$ because of the symmetry of the initial pp state.

The photon rapidity distribution in the parton center of mass frame, $|y^*_\gamma|$, is shown in Figs. 14 and 15. This variable was studied in Ref. [3] for the $W\gamma$ Born process and was found to be quite sensitive to anomalous couplings in the $WW\gamma$ vertex. The dip at $|y^*_\gamma| = 0$ in the $W^+\gamma$ Born result is due to the amplitude zero. Anomalous couplings at the $WW\gamma$ vertex will fill in this dip [3].

Figure 16 shows the invariant mass distribution of the $V\gamma$ pair in the processes $p\bar{p} \to V\gamma + X$ at the Tevatron energy. The invariant mass of the $W\gamma$ pair is not readily measurable since the W boson must be identified by

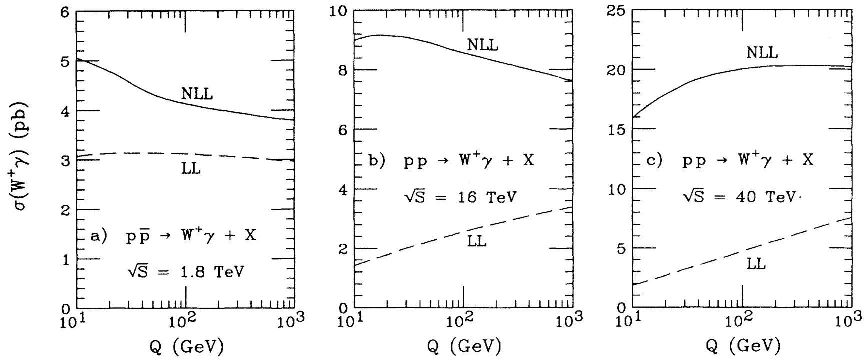

FIG. 9. Same as Fig. 8 but for $W^+\gamma$ production.

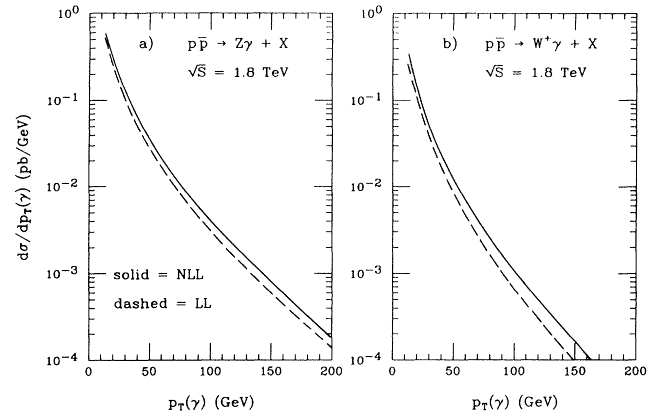

FIG. 10. Transverse momentum distribution of the photon in the reaction $p\bar{p} \rightarrow V\gamma + X$ at the Tevatron energy; parts (a) and (b) are for $Z\gamma$ and $W^{+}\gamma$ production, respectively. The solid curve is the NLL result and the dashed curve is the LL result.

its leptonic decay, $W \rightarrow e\nu$, and the longitudinal momentum of the neutrino is unknown. However, the transverse mass of the $W\gamma$ pair can be measured since only transverse variables are involved. The invariant masses are shown here in both cases so that the $Z\gamma$ and $W^{+}\gamma$ results can be compared. The low invariant-mass tail in the NLL result is due to three-body events in which the V boson and photon are nearly collinear. The invariant mass distributions at the SSC energy are shown in Fig. 17.

These figures show that the order-α_s corrections are larger at large-$p_T(\gamma)$, large-$M_{V\gamma}$, and small-$|y^*_\gamma|$ values. Thus in general, the order-α_s corrections do not simply change the overall normalizations, but instead they also change the shapes of kinematic distributions. These shape changes are due to the presence of three-body final states in the order-α_s cross section.

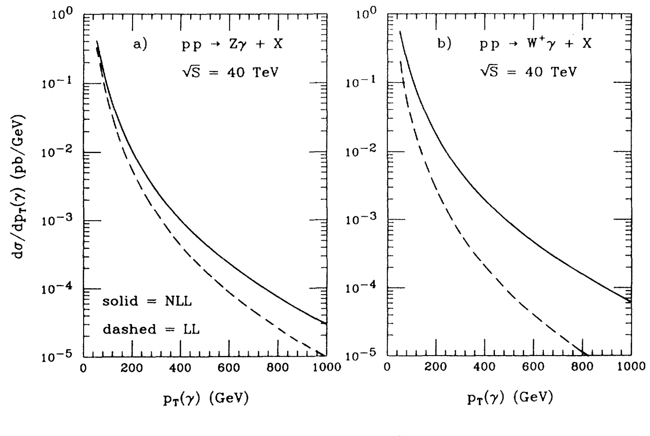

FIG. 11. Same as Fig. 10 but for the reaction $pp \rightarrow V\gamma + X$ at the SSC energy.

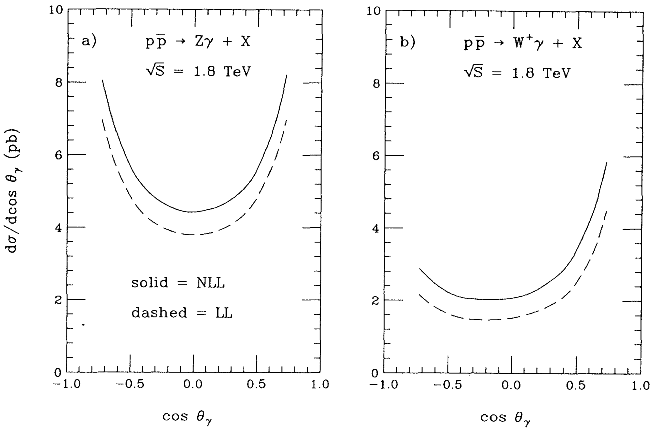

FIG. 12. Distribution of $\cos\theta_\gamma$ in the laboratory frame for the reaction $p\bar{p} \rightarrow V\gamma + X$ at the Tevatron energy; parts (a) and (b) are for $Z\gamma$ and $W^{+}\gamma$ production, respectively. The solid curve is the NLL result and the dashed curve is the LL result.

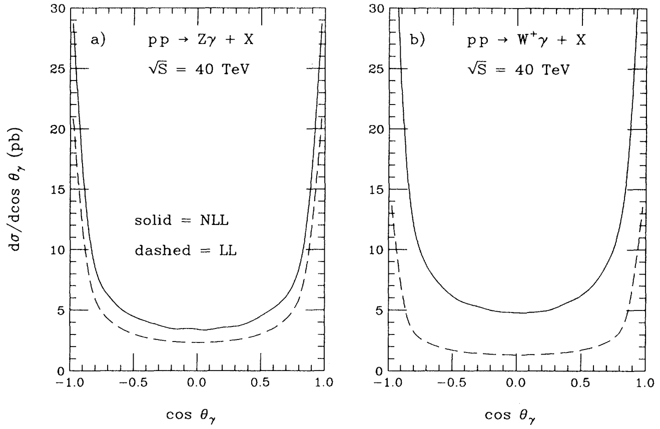

FIG. 13. Same as Fig. 12 but for the reaction $pp \rightarrow V\gamma + X$ at the SSC energy.

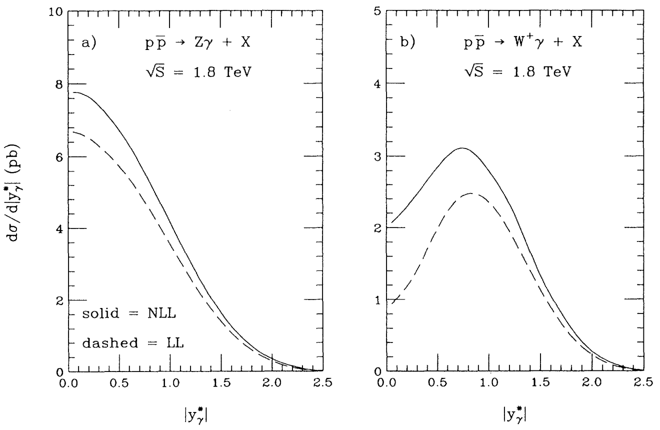

FIG. 14. Rapidity distribution of the photon in the parton center-of-mass frame for the reaction $p\bar{p} \rightarrow V\gamma + X$ at the Tevatron energy; parts (a) and (b) are for $Z\gamma$ and $W^{+}\gamma$ production, respectively. The solid curve is the NLL result and the dashed curve is the LL result.

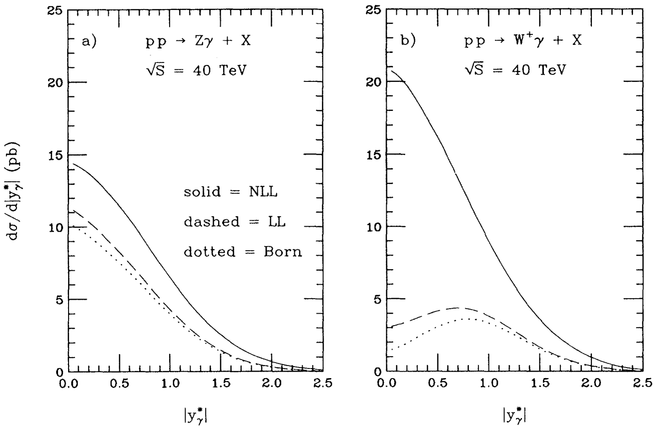

FIG. 15. Same as Fig. 14 but for the reaction $pp \to V\gamma{+}X$ at the SSC energy. The solid curve is the NLL result, the dashed curve is the LL result, and the dotted curve is the Born result.

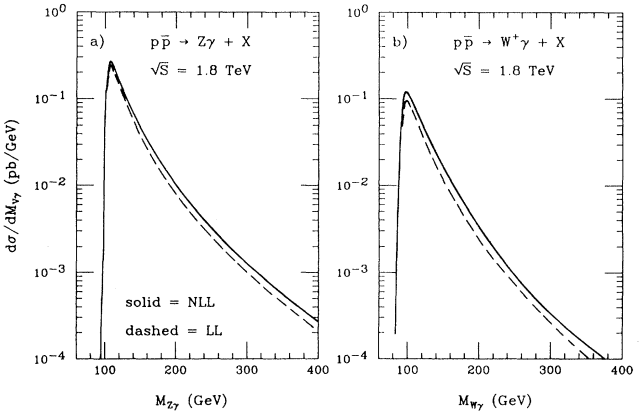

FIG. 16. Invariant mass distribution of the $V\gamma$ pair for the reaction $p\bar{p} \to V\gamma + X$ at the Tevatron energy; parts (a) and (b) are for $Z\gamma$ and $W^{+}\gamma$ production, respectively. The solid curve is the NLL result and the dashed curve is the LL result.

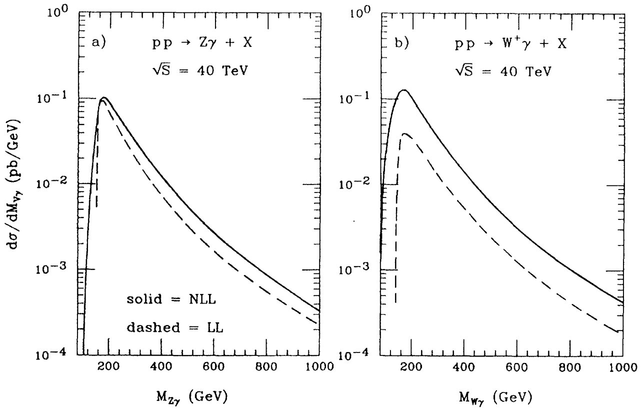

FIG. 17. Same as Fig. 16 but for the reaction $pp \to V\gamma{+}X$ at the SSC energy.

V. SUMMARY

Complete order-α_s calculations of $p\overset{(-)}{p} \to W^{\pm}\gamma$ and $p\overset{(-)}{p} \to Z\gamma$ have been presented. The bulk of the radiative corrections in both cases is due to the opening of the $qg \to V\gamma + X$ production process at order α_s and to the large gluon luminosity at large center-of-mass energies. At the SSC energy, the radiative corrections for $Z\gamma$ production are approximately 40% as large as the Born cross section; however, for $W\gamma$ production the radiative corrections are about twice as large as the Born cross section. The quantitative difference between the radiative corrections to $Z\gamma$ and $W\gamma$ production is attributed to the destructive interference from the s-channel diagram in the $W\gamma$ Born subprocess. This is the same destructive interference that is responsible for the radiation amplitude zero in the $W\gamma$ subprocess. It is imperative that these large radiative corrections be taken into account when measurements at hadron supercolliders are used to test the $WW\gamma$ coupling or the compositeness of the Z boson.

ACKNOWLEDGMENTS

The author wishes to thank U. Baur and W. J. Stirling for useful discussions and comments on this manuscript. Thanks also go to J. Smith and S. Mendoza for assistance in making comparisons with the results of Ref. [17]. Special thanks go to J. F. Owens for his invaluable help during the course of this project. The author also wishes to thank the Florida State University High Energy Physics group for the use of their computing facilities. This research was supported by the U.K. Science and Engineering Research Council.

APPENDIX A: PHOTON BREMSSTRAHLUNG

The photon bremsstrahlung contribution to $V\gamma$ production is calculated by convoluting the order-α_s hard scattering subprocess cross section for V production with the appropriate parton distribution and fragmentation functions:

$$\sigma_{\text{brem}} = \sum_{a,b,c} \int G_{a/A}(x_a, M^2)\, G_{b/B}(x_b, M^2) \times D_{\gamma/c}(z_c, M^2) \times \frac{d\hat{\sigma}}{dv}(ab \to cV)\, dx_a\, dx_b\, dz_c\, dv\,. \tag{A1}$$

The squared matrix element for the subprocess $q_1(p_1) + \bar{q}_2(p_2) \to V(p_3) + g(p_4)$ is

$$\left|\mathcal{M}(q_1\bar{q}_2 \to Vg)\right|^2 = 2^8\, \pi^2\, \alpha\, \alpha_s \left[\left|g_-^{q_1 V q_2}\right|^2 + \left|g_+^{q_1 V q_2}\right|^2\right] \times \left[\frac{t^2 + u^2 + 2sM_V^2}{tu}\right], \tag{A2}$$

where $s = (p_1 + p_2)^2$, $t = (p_1 - p_3)^2$, and $u = (p_1 - p_4)^2$;

spin and color averages are not included. The squared matrix elements for the subprocesses $q_1 g \to Vq_2$ and $g\bar{q}_2 \to V\bar{q}_1$ are obtained by crossing $s \leftrightarrow u$ and $s \leftrightarrow t$, respectively, and introducing an overall minus sign. If a photon isolation cut of the type discussed in Sec. IV is included, then the range of z is reduced from $0 \leq z \leq 1$ to $\frac{1}{1+\epsilon_h} \leq z \leq 1$.

The LL bremsstrahlung cross section is obtained by using leading-log fragmentation functions. The numerical work in this paper was done using the parametrizations of Ref. [39] for the LL fragmentation functions:

$$zD^{\rm LL}_{\gamma/q}(z,Q^2) = F\left[\frac{e_q^2(2.21 - 1.28z + 1.29z^2)z^{0.049}}{1 - 1.63\ln(1-z)} \right. \\ \left. +0.0020(1-z)^{2.0}z^{-1.54}\right], \qquad \text{(A3)}$$

$$zD^{\rm LL}_{\gamma/g}(z,Q^2) = \frac{0.194}{8}\,F\,(1-z)^{1.03}\,z^{-0.97}, \qquad \text{(A4)}$$

where $F = (\alpha/2\pi)\ln(Q^2/\Lambda^2)$ and $\Lambda = \Lambda_4$. These fragmentation functions are proportional to $\alpha\ln(Q^2/\Lambda^2)$; thus they are proportional to α/α_s since $\alpha_s(Q^2) = 12\pi/[(33-2N_F)\ln(Q^2/\Lambda^2)]$. The logarithmic growth of these fragmentation functions arises from an integration over the transverse momentum of the photon with respect to the quark. The upper limit for this integration has been taken to be the typical hard scattering momentum scale Q^2. The divergence associated with the lower limit has been regulated by using the QCD scale parameter Λ as an infrared cutoff. Details on the derivation of these fragmentation functions can be found in Refs. [29] and [39].

At the next-to-leading-log level there are collinear singularities associated with final-state bremsstrahlung which must be factorized and absorbed into fragmentation functions. This will modify the leading-log quark fragmentation functions such that

$$D^{\rm NLL}_{\gamma/q}(z) = D^{\rm LL}_{\gamma/q}(z) + \frac{\alpha}{2\pi}\left[P_{\gamma q}(z)\ln\left\{z(1-z)\delta_c\frac{s}{M^2}\right\} \right. \\ \left. -P'_{\gamma q}(z)\right], \qquad \text{(A5)}$$

(the gluon fragmentation function is unchanged). The new term is the remnant of the collinear singularity after the factorization process has been performed. The functions $P_{\gamma q}(z)$ and $P'_{\gamma q}(z)$ are

$$P_{\gamma q}(z) = Q_q^2\left[\frac{1+(1-z)^2}{z}\right], \qquad \text{(A6)}$$

$$P'_{\gamma q}(z) = -Q_q^2\,z\,. \qquad \text{(A7)}$$

APPENDIX B: LOOP INTEGRALS

Four loop integrals which appear in the $V\gamma$ calculations are given in this appendix. The other loop integrals which appear in the calculation can be found in Refs. [18] and [19].

The integrals were evaluated using the Feynman parametrization technique and dimensional regularization was used to regularize the integrals. The number of space-time dimensions has been set to $N = 4 - 2\epsilon$. The integrals are written with a common factor

$$F = \left(\frac{4\pi}{s}\right)^{\epsilon}\frac{\Gamma(1-\epsilon)}{\Gamma(1-2\epsilon)}\frac{1}{(4\pi)^2}\,. \qquad \text{(B1)}$$

The four integrals are

$$I_1 \equiv \int\frac{d^Nk}{(2\pi)^N}\,\frac{1}{k^2(k+p_1)^2(k+p_1-p_3)^2(k-p_2)^2}$$
$$= i\frac{2F}{st}\left[\frac{1}{\epsilon^2} - \frac{1}{\epsilon}\ln\left(\frac{-t}{M_W^2}\right) + \frac{1}{2}\ln\left(\frac{-t}{M_W^2}\right)^2 + {\rm Li}_2\left(1-\frac{s}{M_W^2}\right) + {\rm Li}_2\left(1-\frac{t}{M_W^2}\right)\right],$$

$$I_2^{\mu\nu} \equiv \int\frac{d^Nk}{(2\pi)^N}\,\frac{k^\mu k^\nu}{k^2(k+a)^2(k+b)^2}\,, \quad a^2 \neq 0, b^2 = 0, (a-b)^2 = 0,$$
$$= i\frac{F}{2a^2}\left[b^\mu b^\nu\left\{\frac{2}{\epsilon^2} + \frac{3}{\epsilon} - \frac{2}{\epsilon}\ln\left(\frac{-a^2}{s}\right) + 6 + \frac{\pi^2}{3} - 3\ln\left(\frac{-a^2}{s}\right) + \ln\left(\frac{-a^2}{s}\right)^2\right\}\right.$$
$$-\left\{b^\mu(a^\nu - b^\nu) + b^\nu(a^\mu - b^\mu)\right\}\left\{\frac{2}{\epsilon} + 5 - 2\ln\left(\frac{-a^2}{s}\right)\right\}$$
$$\left.-(a^\mu - b^\mu)(a^\nu - b^\nu)\left\{\frac{1}{\epsilon} + 2 - \ln\left(\frac{-a^2}{s}\right)\right\} + g^{\mu\nu}\frac{a^2}{2}\left\{\frac{1}{\epsilon} + 3 - \ln\left(\frac{-a^2}{s}\right)\right\}\right],$$

$$I_3^{\mu} \equiv \int\frac{d^Nk}{(2\pi)^N}\,\frac{k^\mu}{k^2(k+a)^2(k+b)^2}\,, \quad a^2 \neq 0, b^2 = 0, (a-b)^2 = 0,$$
$$= i\frac{F}{a^2}\left[a^\mu\left\{\frac{1}{\epsilon} - 2 - \ln\left(\frac{-a^2}{s}\right)\right\}\right.$$
$$\left.-b^\mu\left\{\frac{1}{\epsilon^2} + \frac{2}{\epsilon} - \frac{1}{\epsilon}\ln\left(\frac{-a^2}{s}\right) + 4 + \frac{\pi^2}{6} - 2\ln\left(\frac{-a^2}{s}\right) + \frac{1}{2}\ln\left(\frac{-a^2}{s}\right)^2\right\}\right],$$

$$I_4 \equiv \int \frac{d^N k}{(2\pi)^N} \frac{1}{k^2(k+a)^2(k+b)^2}\,, \quad a^2 \neq 0, b^2 = 0, (a-b)^2 = 0,$$
$$= i\frac{F}{a^2}\left[\frac{1}{\epsilon^2} - \frac{1}{\epsilon}\ln\left(\frac{-a^2}{s}\right) + \frac{1}{2}\ln\left(\frac{-a^2}{s}\right)^2 + \frac{\pi^2}{6}\right].$$

The function $\mathrm{Li}_2(z)$ is the dilogarithm function

$$\mathrm{Li}_2(z) = -\int_0^1 \ln(1-tz)\frac{dt}{t} = \sum_{k=1}^{\infty}\frac{z^k}{k^2}\,. \tag{B2}$$

APPENDIX C: REAL EMISSION SUBPROCESSES

The Feynman diagrams which contribute to the amplitude for the real emission subprocess

$$q(p_1) + \bar{q}(p_2) \longrightarrow Z(p_3) + \gamma(p_4) + g(p_5) \tag{C1}$$

are shown in Fig. 3. The squared amplitude summed over final-state polarizations and initial-state spins can be written

$$\left|\mathcal{M}^{\mathrm{real}}\right|^2 = 4\pi\alpha_s\,(4\pi\alpha)^2\,Q_q^2\left(\frac{N_C^2-1}{2}\right)\left[\left(g_-^{qZq}\right)^2 + \left(g_+^{qZq}\right)^2\right]\sum_{\substack{i=1,6\\ j=i,6}} M_{ij}\,. \tag{C2}$$

The M_{ij} are functions of the Z-boson mass M_Z and the Lorentz scalars $s_{ij} = (p_i + p_j)^2$ and $t_{ij} = (p_i - p_j)^2$:

$$\begin{aligned}
M_{11} &= \frac{8s_{45}}{t_{15}t_{24}}\,,\\
M_{12} &= \frac{16t_{25}}{t_{15}t_{23}t_{24}}\left[M_Z^2 - t_{15}\right],\\
M_{13} &= \frac{8}{t_{13}t_{15}t_{24}t_{25}}\left[2s_{12}(t_{14}t_{24} - t_{15}t_{25}) + s_{12}s_{45}(t_{14} - t_{15} + t_{24}) + (t_{14} + t_{15} - t_{24})(t_{15}t_{24} - t_{14}t_{25})\right],\\
M_{14} &= \frac{16s_{12}}{t_{14}t_{15}t_{24}t_{25}}\left[s_{12}(M_Z^2 - s_{45}) + (t_{14} + t_{24})(t_{15} + t_{25})\right],\\
M_{22} &= \frac{8}{t_{15}t_{23}^2}\left[(s_{12} + t_{24})(t_{15} + s_{45}) - t_{14}t_{25}\right],\\
M_{23} &= \frac{16s_{12}}{t_{13}t_{15}t_{23}t_{25}}\left[s_{12} + t_{15} + t_{15}\right]\left[M_Z^2 + s_{45}\right],\\
M_{25} &= \frac{8}{t_{13}t_{15}t_{23}t_{24}}\Big[2s_{12}(t_{14} + t_{25} + s_{12})(t_{14} + t_{25} + s_{12} + s_{45}) + (t_{14} + t_{25} + s_{45})(s_{12}s_{45} + t_{14}t_{25} - t_{15}t_{24})\\
&\qquad +2s_{12}\{t_{15}(s_{12} + t_{14}) + t_{24}(s_{12} + t_{25}) + s_{12}s_{45} - t_{15}t_{24}\}\Big],\\
M_{26} &= \frac{16}{t_{14}t_{15}t_{23}^2}\left[t_{14} + t_{15} + s_{45}\right]\left[s_{12}s_{45} - (t_{14} + t_{15})(t_{24} + t_{25})\right].
\end{aligned}$$

The remaining M_{ij} expressions are related to the above expressions by interchanging parton momenta:

$$\begin{aligned}
&M_{15} = M_{12}(1 \leftrightarrow 2, 4 \leftrightarrow 5), \quad M_{24} = M_{13}(1 \leftrightarrow 2), \quad M_{33} = M_{22}(1 \leftrightarrow 2),\\
&M_{16} = M_{13}(1 \leftrightarrow 2, 4 \leftrightarrow 5), \quad M_{34} = M_{12}(1 \leftrightarrow 2), \quad M_{35} = M_{26}(1 \leftrightarrow 2),\\
&M_{55} = M_{22}(1 \leftrightarrow 2, 4 \leftrightarrow 5), \quad M_{36} = M_{25}(1 \leftrightarrow 2), \quad M_{44} = M_{11}(1 \leftrightarrow 2),\\
&M_{45} = M_{13}(4 \leftrightarrow 5), \quad M_{46} = M_{12}(4 \leftrightarrow 5), \quad M_{56} = M_{23}(4 \leftrightarrow 5), \quad M_{66} = M_{22}(4 \leftrightarrow 5).
\end{aligned}$$

The squared amplitudes for the subprocesses $qg \to Z\gamma q$ and $g\bar{q} \to Z\gamma\bar{q}$ can be obtained from the $q\bar{q} \to Z\gamma g$ squared amplitude by crossing $p_2 \leftrightarrow -p_5$ and $p_1 \leftrightarrow -p_5$, respectively. Furthermore, one has to correct for an overall minus sign and change the color average from $\frac{1}{3} \times \frac{1}{3}$ to $\frac{1}{3} \times \frac{1}{8}$. The subprocess cross section is

$$d\hat{\sigma}(q\bar{q} \to Z\gamma g) = \frac{1}{4}A_C\,\frac{1}{2s_{12}}\,|\mathcal{M}|^2\,d^4\Phi_3\,, \tag{C3}$$

where the factors $\frac{1}{4}$ and A_C are the spin and color average, respectively.

[1] E. Eichten, I. Hinchliffe, K. Lane, and C. Quigg, Rev. Mod. Phys. **56**, 579 (1984); **58**, 1065(E) (1986).

[2] J. Cortes, K. Hagiwara, and F. Herzog, Nucl. Phys. **B278**, 26 (1986).

[3] U. Baur and D. Zeppenfeld, Nucl. Phys. **B308**, 127 (1988).

[4] H. Kuijf *et al.*, in *Proceedings of the ECFA Large Hadron Collider Workshop*, Aachen, Germany, 1990, edited by G. Jarlskog and D. Rein (CERN Report No. 90-10, Geneva, Switzerland, 1990), Vol. II, p. 91,

[5] M. Leurer, H. Harari, and R. Barbieri, Phys. Lett. **141B**, 455 (1985).

[6] R. W. Brown, K. O. Mikaelian, and D. Sahdev, Phys. Rev. D **20**, 1164 (1979); K. O. Mikaelian, M. A. Samuel, and D. Sahdev, Phys. Rev. Lett. **43**, 746 (1979).

[7] F. Renard, Nucl. Phys. **B196**, 93 (1982).

[8] S. J. Brodsky and R. W. Brown, Phys. Rev. Lett. **49**, 966 (1982); M. A. Samuel, Phys. Rev. D **27**, 2724 (1983); R. W. Brown, K. L. Kowalski, and S. J. Brodsky, *ibid.* **28**, 624 (1983).

[9] U. Baur and D. Zeppenfeld, Nucl. Phys. **B325**, 253 (1989); U. Baur *et al.*, in *Proceedings of the ECFA Large Hadron Collider Workshop* [4], Vol. II, p. 956; U. Baur, J. A. M. Vermaseren, and D. Zeppenfeld, Nucl. Phys. **B375**, 3 (1992); U. Baur and M. A. Doncheski, Phys. Rev. D **46**, 1959 (1992).

[10] K. Hagiwara, R. D. Peccei, D. Zeppenfeld, and K. Hikasa, Nucl. Phys. **B282**, 253 (1987); D. Zeppenfeld, Phys. Lett. B **183**, 380 (1987).

[11] UA2 Collaboration, J. Alitti *et al.*, Phys. Lett. B **277**, 194 (1992).

[12] G. Li, M. A. Samuel, N. Sinha, R. Sinha, and M. K. Sundaresan, Phys. Lett. B **280**, 124 (1992); G. Li, M. A. Samuel, N. Sinha, and M. K. Sundaresan, Phys. Rev. Lett. **67**, 9 (1991).

[13] U. Baur, E. W. N. Glover, and J. J. van der Bij, Nucl. Phys. **B318**, 106 (1989).

[14] V. Barger, T. Han, J. Ohnemus, and D. Zeppenfeld, Phys. Rev. D **41**, 2782 (1990).

[15] Ll. Ametller, E. Gava, N. Paver, and D. Treleani, Phys. Rev. D **32**, 1699 (1985).

[16] J. J. van der Bij and E. W. N. Glover, Phys. Lett. B **206**, 701 (1988).

[17] J. Smith, D. Thomas, and W. L. van Neerven, Z. Phys. C **44**, 267 (1989).

[18] J. Ohnemus and J. F. Owens, Phys. Rev. D **43**, 3626 (1991).

[19] J. Ohnemus, Phys. Rev. D **44**, 1403 (1991).

[20] J. Ohnemus, Phys. Rev. D **44**, 3477 (1991).

[21] B. Bailey, J. Ohnemus, and J. F. Owens, Phys. Rev. D **46**, 2018 (1992).

[22] H. Baer, J. Ohnemus, and J. F. Owens, Phys. Rev. D **42**, 61 (1990); Phys. Lett. B **234**, 127 (1990).

[23] H. Baer, J. Ohnemus, and J. F. Owens, Phys. Rev. D **40**, 2844 (1989).

[24] L. Bergmann, Ph.D. dissertation, Florida State University Report No. FSU-HEP-890215, 1989 (unpublished).

[25] H. Baer and M. H. Reno, Phys. Rev. D **43**, 2892 (1991).

[26] G. 't Hooft and M. Veltman, Nucl. Phys. **B44**, 189 (1972).

[27] B. Mele, P. Nason, and G. Ridolfi, Nucl. Phys. **B357**, 409 (1991).

[28] FORM is a computer algebra program written by J. A. M. Vermaseren (unpublished).

[29] J. F. Owens, Rev. Mod. Phys. **59**, 465 (1987).

[30] W. A. Bardeen, A. J. Buras, D. W. Duke, and T. Muta, Phys. Rev. D **18**, 3998 (1978).

[31] J. F. Owens and W. K. Tung, Annu. Rev. Nucl. Part. Sci. (to be published).

[32] Recent measurements of the Z widths and the W and Z masses indicate that the top-quark mass is most likely to be around 140 GeV. See, for example, U. Amaldi, A. Böhm, L. S. Durkin, P. Langacker, A. K. Mann, W. J. Marciano, A. Sirlin, and H. H. Williams, Phys. Rev. D **36**, 1385 (1987); G. Costa, J. Ellis, G. L. Fogli, D. V. Nanopoulos, and F. Zwirner, Nucl. Phys. **B297**, 244 (1988); J. Ellis and G. Fogli, Phys. Lett. B **213**, 526 (1989); V. Barger, J. Hewett, and T. Rizzo, Phys. Rev. Lett. **65**, 1313 (1990).

[33] CDF Collaboration, F. Abe *et al.*, Phys. Rev. Lett. **63**, 720 (1989).

[34] Mark II Collaboration, G. S. Abrams *et al.*, Phys. Rev. Lett. **63**, 724 (1989).

[35] ALEPH Collaboration, D. Decamp *et al.*, Phys. Lett. B **231**, 519 (1989); **235**, 399 (1990); DELPHI Collaboration, P. Aarnio *et al.*, *ibid.* **231**, 539 (1989); L3 Collaboration, B. Adeva *et al.*, *ibid.* **231**, 509 (1989); OPAL Collaboration, M. Z. Akrawy *et al.*, *ibid.* **231**, 530 (1989).

[36] J. Smith (private communication).

[37] S. Mendoza, J. Smith, and W. L. van Neerven (in progress).

[38] P. N. Harriman, A. D. Martin, R. G. Roberts, and W. J. Stirling, Phys. Rev. D **42**, 798 (1990).

[39] D. W. Duke and J. F. Owens, Phys. Rev. D **26**, 1600 (1982).